ACS Photonics

pubs.acs.org/journal/apchd5 Letter

All-Epitaxial Integration of Long-Wavelength Infrared Plasmonic Materials and Detectors for Enhanced Responsivity

Leland Nordin, Abhilasha Kamboj, Priyanka Petluru, Eric Shaner, and Daniel Wasserman*

Cite This: https://dx.doi.org/10.1021/acsphotonics.0c00659 **Read Online**

ACCESS | Metrics & More | Article Recommendations | SI Supporting Information

ABSTRACT: Infrared detectors using monolithically integrated doped semiconductor "designer metals" are proposed and experimentally demonstrated. We leverage the "designer metal" groundplanes to form resonant cavities with enhanced absorption tuned across the long-wave infrared (LWIR). Detectors are designed with two target absorption enhancement wavelengths: 8 and 10 μm. The core of our detectors are quantum-engineered LWIR type-II superlattice p-i-n detectors with total thicknesses of only 1.42 and 1.80 μm for the 8 and 10 μm absorption enhancement devices, respectively. Our 8 and 10 μm structures show peak external quantum efficiencies of 45 and 27%, which are 4.5× and 2.7× enhanced, respectively, compared to control structures. We demonstrate the clear advantages of this detector architecture, both in terms of ease of growth/fabrication and enhanced device performance. The proposed architecture is absorber- and device-structure agnostic, much thinner than state-of-the-art LWIR T2SLs, and offers the opportunity for the integration of low dark current LWIR detector architectures for significant enhancement of IR detectivity.

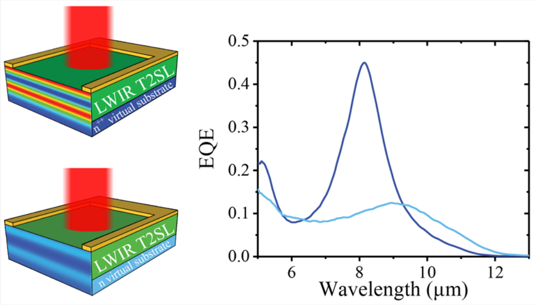

KEYWORDS: *superlattices, epitaxy, plasmonic, mid-infrared, photodetector, semiconductor*

The mid-infrared (mid-IR) has emerged as a vital wavelength range for a wide variety of defense, sensing, and fundamental science applications. While the development of the quantum and interband cascade lasers revolutionized mid-IR sources, the "state-of-the-art" mid-IR detector remains the HgCdTe (MCT) photodiode, unchanged for the past 4 or 5 decades. Recently, the type-II superlattice (T2SL) has been proposed as a potential replacement for the HgCdTe material system.[1,2] T2SLs consist of alternating layers of semiconductors with type-II band offsets, which form superlattice minibands with effective band-gaps, tunable both by the choice of materials and the thickness of each nanoscale layer. Mid-IR detector structures using T2SL materials allow for widely tunable (3−30 μm) absorption and are predicted to be able to achieve improved performance over MCT.[3] T2SL detectors are most often grown by molecular beam epitaxy (MBE), offering excellent uniformity on relatively affordable GaSb or InAs substrates. Typical T2SL detectors have weaker absorption than bulk alloys with similar cutoff wavelengths and, thus, require thick absorber layers (multiple microns) to achieve the equivalent responsivity as a bulk material with the same cutoff wavelength.[4−7] The thicker absorbers required for the T2SL-based detectors increases the cost of detector growth, as well as decreases tolerance for strain accumulation due to lattice mismatch over the course of the hundreds of epitaxial layers which comprise a typical T2SL absorber region. Even were these materials to be grown perfectly lattice-matched, the use of thicker absorber layers is not a panacea for the weaker T2SL absorption. First, the finite diffusion length of photogenerated carriers reduces the probability of collection for carriers excited farther from the collector junction of a detector. Thus, while increasing the thickness of the T2SL absorber layers can boost the overall absorption efficiency of the T2SL, each additional absorbed photon is less likely to be collected as current. In addition, thicker absorber layers also introduce greater detector dark current, which for a diffusion limited detector, scales as[3]

$$J_{\mathrm{diff}} = q\frac{n_{\mathrm{i}}^{2}d}{n_{0}\tau_{\mathrm{mc}}}$$

where q is the electron charge, n_{i} is the intrinsic carrier concentration, d is the detector thickness, n_0 is the electron density, and τ_{mc} is the minority carrier lifetime. Therefore, the detector thickness is directly proportional to the dark current in a diffusion-limited detector. For high-temperature operation low dark current is necessary as the intrinsic dark current

Received: April 22, 2020
Published: July 4, 2020

ultimately determines the detectors' background-limited performance.

There is thus significant motivation to design either detector materials, or detector architectures, which are capable of strong absorption in thin ($\lesssim 2\ \mu$m) absorber regions. While the absorption cutoff of typical T2SL materials can be spectrally engineered, it can be more difficult to control the magnitude of the absorption coefficient, for a given cutoff wavelength, without adversely affecting the diffusion length of the minority carriers in the T2SL. This trade-off is a result of the stronger overlap between electron and hole wave functions in the semiconductor superlattice required to increase the T2SL absorption coefficient. Such wave function engineering has, as an unwelcome consequence, increased recombination rates and decreased vertical mobility due to the greater localization of the charge carrier wave functions, both of which will decrease minority carrier diffusion lengths.[8,9] However, for a given absorber design, the effective absorption coefficient can be increased by engineering the optical, not electronic, structure of the detector, increasing the interaction of incident light with the absorber. Previous work on thin T2SL detectors has leveraged plasmonic modes, metasurfaces, grating modes, or distributed Bragg reflectors[10−14] in order to locally enhance the overlap of the incident light's field with the T2SL absorber material. In most cases, such approaches require either significant additional growth (Bragg reflectors) or complicated fabrication protocols, including grating fabrication, surface patterning, or even substrate removal and metallization both above and below the micron-scale thickness T2SL.

In this work we propose an architecture for long-wavelength infrared (LWIR) detector absorption enhancement which requires no additional fabrication or patterning processes. Our device architecture leverages monolithic integration of LWIR absorber materials with epitaxially grown doped semiconductor plasmonic "designer metals" to create a resonant cavity enhancement (RCE) detector.[15] Doped semiconductors are a particularly intriguing material for mid-IR plasmonic applications; for high doping concentrations and small effective masses, doped semiconductors can behave as mid-IR plasmonic materials with optical response obeying the Drude formalism. These "designer metals", when epitaxially grown, offer control over the spectral range of plasmonic behavior,[16−18] as well as control over the dimensions and doping profile of the plasmonic layers with the atomic precision of MBE. Perhaps most importantly these heavily doped semiconductors offer the potential for monolithic integration of plasmonic materials with not only mid-IR quantum engineered emitters,[19] but as we show here, optoelectronic device architectures.[20] We numerically simulate and experimentally demonstrate significant absorption enhancement in thin LWIR detectors, resulting in detector efficiencies commensurate with those of much thicker detectors found in the literature. Our approach provides a demonstration of the potential for monolithically integrated semiconductor plasmonics and optoelectronics at LWIR wavelengths and opens the door to a range of hybrid plasmonic/optoelectronic devices for LWIR applications.

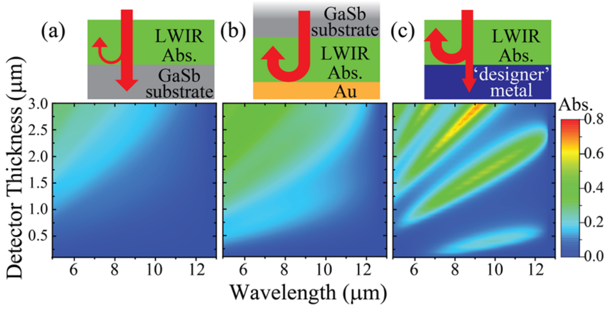

Figure 1. Simulated absorption for three different detector architectures as a function of detector thickness and wavelength. Simulated absorption and detector stack for (a) a LWIR absorber grown on a dielectric substrate, (b) the same structure, with the top surface Au-metallized and the detector "flip-chipped" and illuminated through the substrate, and (c) our monolithically integrated plasmonic implementation. Both the metallized and substrate illuminated and the proposed monolithically integrated plasmonic groundplane devices have better performance than the simple LWIR absorber grown on a dielectric substrate. However, the architecture shown and modeled in (c) has significantly better performance in the LWIR, particularly for thin cavities (d = 1−2 μm).

Shown in Figure 1a is the simulated absorption from a LWIR detector, for a range of absorber thicknesses ($0.1 < d < 3.0\ \mu$m), grown on a semiconductor substrate, as is typical for single element detectors. In such a system, absorption efficiency is weak (<40%) even at short wavelengths and effectively nonexistent in the LWIR. Alternatively, enhanced absorption can be achieved by "flip-chipping" the sample, metallizing the epitaxially grown surface and bonding the metallized surface, substrate up, to a carrier wafer. In such a configuration, light is incident from the backside of the device, through the semiconductor substrate. The metallized groundplane then effectively provides a "double-pass" configuration for enhanced absorption in the detector due to the high reflectivity of the metal in the LWIR. Figure 1b shows the simulated absorption for the metallized top surface detector, with the same absorber modeled in Figure 1a, assuming a lossless substrate, an assumption that may significantly overestimate the actual absorption in such a configuration, given the non-negligible losses in typical LWIR detector substrates.[21] As expected, the absorption in Figure 1b is enhanced relative to the traditional as-grown structure (Figure 1a). However, thick detector structures (>3 μm) are still required to achieve even ∼40% absorption in the technologically relevant 8−12 μm region.[22] To overcome this thickness limit we propose a monolithically integrated doped semiconductor groundplane with a plasma wavelength (λ_p) in the mid-infrared. The highly doped semiconductor, for $\lambda > \lambda_p$, will have a negative permittivity (see Methods) and, thus, high reflectivity at the virtual substrate/T2SL interface. For a given T2SL thickness, the three-layer system (virtual substrate/T2SL/air) will form a leaky cavity, resulting in strong field confinement, a minimum in the reflection spectrum, and enhanced absorption. Shown in Figure 1c is the geometry and the simulated absorption spectra of our proposed architecture, assuming a "designer metal" with plasma wavelength $\lambda_p = 7\ \mu$m and scattering rate $\tau = 1 \times 10^{13}$, in line with typical parameters for heavily doped semiconductors.[17,18,23] Notably, absorption >40% is predicted for detector thicknesses on the order of 1−1.5 μm, much thinner than the ∼2.5 μm needed for the same absorption in the flip chipped implementation. The absorption feature for the doped groundplane configuration, while localized spectrally, is broad enough to provide significantly enhanced absorption across the entire LWIR. Additionally, the detector configuration in Figure 1c can be implemented all-epitaxially, meaning that no extraordinary fabrication methods are required to achieve the enhanced absorption.

In order to implement and demonstrate the effectiveness of the proposed architecture, we grow p-i-n T2SL detectors of two different cavity thicknesses, targeting 8 and 10 μm absorption enhancement, with two different "virtual substrates", one heavily n-type doped (n^{++}) and one more lightly doped (n), for each detector thickness. We demonstrate significant absorption enhancement in our n^{++} devices, compared to the more lightly doped n devices, and demonstrate control over the spectral enhancement by choice of T2SL thickness (d). Our results are compared to numerical simulations with excellent agreement.

■ RESULTS AND DISCUSSION

The growth, fabrication, characterization, and modeling of our detectors is primarily described in the Methods section. Our architecture is effectively the doped semiconductor structure shown in Figure 1c: an absorber region grown above a n^{++} designer metal virtual substrate. The absorber thicknesses above the virtual substrate are engineered to form resonant cavities at 8 μm (d = 1.42 μm) and 10 μm (d = 1.80 μm). To quantify the achievable absorption enhancement, we also grow control structures which mirror each of the n^{++} devices, but which replace the n^{++} virtual substrate with a moderately doped n virtual substrate. The device structures and 83 K reflection spectra from both the d = 1.42 μm and d = 1.80 μm n^{++} and n structures are shown in Figure 2. A clear dip in reflection at 8 μm for the d = 1.42 μm detector and at 10 μm for the d = 1.80 μm thick detector are observed for the samples with the n^{++} virtual substrates, corresponding to resonant cavity modes of the dielectric T2SL layer on the plasmonic virtual substrate. Though the samples with the more lightly doped virtual substrates also show reflection dips, these features are red-shifted and less pronounced, suggesting the presence of a comparatively weak cavity mode associated with the reflection from the dielectric−dielectric interface between the virtual substrate and T2SL (as the virtual substrates of the n detectors have λ_p = 13.1 μm and are thus not optical metals at the cavity resonance).

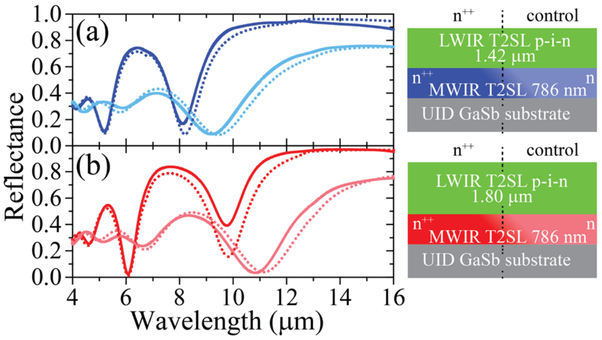

Figure 2. Low temperature (83 K) reflection from the as-grown samples investigated in this work. (a) Reflection from the d = 1.42 μm thick samples with n^{++} (blue) and n (light-blue) virtual substrates targeting λ = 8 μm absorption enhancement. (b) Reflection from the d = 1.80 μm thick samples with n^{++} (red) and n (light-red) virtual substrates targeting λ = 10 μm absorption enhancement. The sample structures are shown to the right of the reflection spectra for that sample. Dotted lines show the simulated reflection from the structures, treating the n^{++} layer as a Drude metal and the absorber with a simple $\alpha(E) = \alpha_0\sqrt{E - E_g}$ dependence, where α_0 = 4500 cm^{-1}. We use half max (fwhm) to the long-wavelength edge of the 83 K photoluminescence (PL) spectrum of the control (n) sample (PL and fit provided in the Supporting Information).

The optical properties of the epitaxial stacks are simulated numerically using a rigorous coupled wave analysis (RCWA) package,[24] in order to understand the mode confinement of each device as a function of incident wavelength. Figure 3 shows the electric field amplitude $|E|^2$ as a function of position in the detector, for the d = 1.42 μm and d = 1.80 μm n^{++} and n devices both on resonance, Figure 3b,d, and off resonance, Figure 3a,c. A significant enhancement of the electric field magnitude is evident for the n^{++} devices on resonance, whereas the n device has approximately the same electric field magnitude for both on and off the n^{++} devices' resonances. The field profiles in Figure 3 indicate that incident light is coupling to a second order ($d \sim 3\lambda/4n$) leaky cavity mode (where n is the index of refraction and d is the thickness of the T2SL). There is the possibility that the additional cavity modes could reduce the radiative lifetime of carriers and as such reduce detector response. However, the radiative lifetime in the specific T2SL system utilized has shown to be long,[25] especially relative to other recombination mechanism times, so it is unlikely that the proposed cavity adversely affects carrier collection. For the p-i-n detectors employed in this work, a non-negligible amount of the total field is present in the p and n contact layers. Photogenerated carriers in these regions are significantly less likely to contribute to the photocurrent, due to the small depletion region in the contacts, the short recombination times in heavily doped LWIR materials,[25] and for the n-contact, the presence of tightly bound surface-plasmon-polariton modes at the n-contact/virtual substrate interface.[19]

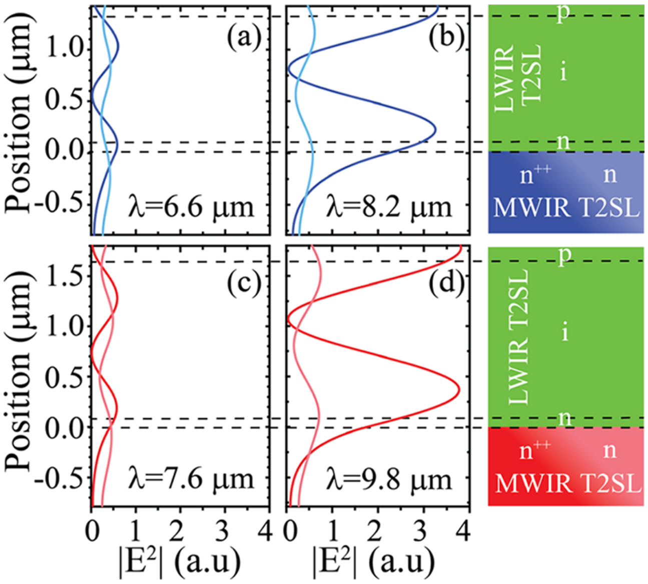

Figure 3. Simulated field profiles for the n^{++} (blue) and n (light-blue) d = 1.42 μm thick detectors (a) off resonance (λ = 6.6 μm) and (b) on resonance (λ = 8.2 μm). Simulated field profiles for the n^{++} (red) and n (light-red) d = 1.80 μm thick detectors (c) off resonance (λ = 7.6 μm) and (d) on resonance (λ = 9.8 μm). The detector stacks are shown to the right of the corresponding field plots.

To predict the expected magnitude of the RCE, we thus simulate absorption in only the i-region of each detector, using the same RCWA model described above. Shown in Figure 4a is the simulated absorption for both n^{++} detectors and their

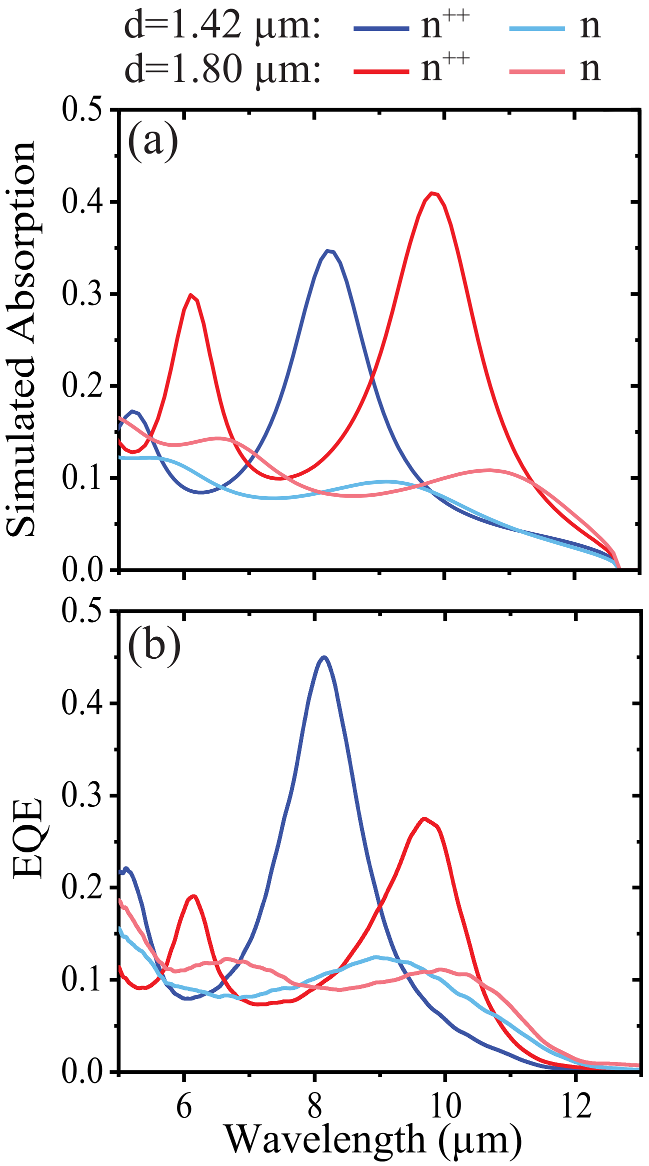

Figure 4. (a) Simulated absorption in the intrinsic region of all of the detectors studied in this work. (b) Experimentally measured EQE of our RCE detectors with their respective controls. Strong enhancement in signal for both the d = 1.42 and 1.80 μm n^{++} detectors is seen across the integrated LWIR and specifically at their design wavelengths.

respective controls. The absorption coefficient used to model the absorber is the same as was used for the simulations shown in Figure 2: $\alpha(E) = \alpha_0\sqrt{E - E_g}$, where E_g = 96.55 meV (12.7 μm), as determined from photoluminescence (PL; see Supporting Information), and α_o = 4500 cm^{-1}, in line with typical absorption coefficients of LWIR T2SL materials.[26] The results of our numerical simulations predict significant absorption enhancement at λ = 8 μm for the d = 1.42 μm thick detector and at λ = 10 μm for the d = 1.80 μm thick detector, with both detectors showing peak absorption nearing 40%. Additionally, we see a clear enhancement in the predicted response of the n^{++} virtual substrate devices when compared to the weak absorption in the moderately doped virtual substrate detectors.

Each of the four detectors' spectral response and responsivity are measured experimentally, see Methods for a thorough description of both experiments, and from this the external quantum efficiency (EQE) for the n^{++} and n detectors are calculated and shown in Figure 4b. The spectral locations of the peak EQEs of both RCE n^{++} detectors are at the designed/simulated wavelengths (Figure 4a), and the peak EQE amplitudes are approximately 4.5× (2.5×) the EQEs of the moderately doped virtual substrate devices for the d = 1.42 μm (d = 1.80 μm) detectors. Additionally, the resonant cavity structures possess comparable response to the moderately doped virtual substrate devices outside of the target enhancement wavelength. The comparable out-of-band response can be simply understood by the fact that the quality factor, and therefore finesse, of our cavity is relatively small due to the low reflectivity of the air/semiconductor interface. To quantify the broadband EQE enhancement, we calculate the broadband enhancement factor (F), which is the ratio of the n^{++} detector's integrated EQE over the moderately doped detector's integrated EQE in the technologically relevant 8−12 μm range, see Methods for integration specifics. We find that F is equal to 1.70 (1.56) for the d = 1.42 μm (d = 1.80 μm) detectors, indicating the broadband EQE of the n^{++} structures are enhanced.

The strongly enhanced response of the photodetectors grown on the n^{++} virtual substrates provides clear evidence for the significant improvement in photodetector operation achievable by direct integration of epitaxial plasmonic materials with IR optoelectronic devices. In this work we use T2SL p-i-n structures as our photodetectors, as they provide a continuous absorber region where we can assume that all photoexcited charge carriers are collected as current. This allows us to compare responsivity for detectors of varying thicknesses and different groundplanes. The current state-of-the-art T2SL generally employs a bariode architecture (nBn[27] or CBIRD[5]), which possess significant advantages in terms of dark current. However, charge collection efficiency for the bariode devices is not uniform across the absorber region (as photoexcited charge carriers must diffuse to the barrier junction). Thus, for a bariode device, the collection efficiency is a convolution of the spatial profiles of the absorption and charge collection efficiency, making comparison of detectors with differing absorber thickness and field profiles more complicated. Future efforts will replace the p-i-n detectors of this work with bariode structures, in order to reap the benefits not only of the enhanced absorption demonstrated here, but the significantly lower dark currents achievable with thin barrier-based photodetector architectures.

■ CONCLUSIONS

We have proposed and demonstrated a photodetector architecture leveraging the monolithic integration of highly doped semiconductor plasmonic materials with quantum engineered LWIR photodetector structures. The use of the doped semiconductor virtual substrates allows for resonant confinement of LWIR light in the detector absorber region, significantly boosting the detector response. Specifically, the use of the monolithic RCE architecture allows for greater absorption efficiency, in thinner absorber layers, than would be possible for detectors grown on traditional semiconductor substrates or even using continuous metal top contacts and backside illumination (the "double-pass" configuration). To demonstrate the achievable absorption enhancement in our proposed architecture, we grew photodetector devices on plasmonic virtual substrates with two different absorber thicknesses, targeting resonant cavity enhancement at $\lambda = 8$ μm and 10 μm. The performance of both detectors are compared to the performance of the same detector structures grown on moderately doped (non-plasmonic) virtual substrates.

Reflection spectra from the $d = 1.42$ and 1.80 μm n^{++} RCE detectors confirms the presence of a cavity resonance at the $\lambda =$ 8 and 10 μm design wavelengths. Numerical simulations of the detectors, on resonance, demonstrate a strong field enhancement for the n^{++} virtual substrate devices, when compared to the devices with the moderate n-doped virtual substrates. These simulations predict a 4× enhancement in absorption for our RCE detectors relative to their moderately doped control devices. Measured EQE of the fabricated detectors verifies a significant (4.5× and 2.5×) peak EQE enhancement, on resonance, for the $d = 1.42$ and 1.80 μm thick detectors at $\lambda =$ 8.2 and 9.8 μm, respectively, compared to their control devices. Because the proposed and demonstrated cavity absorption enhancement is effectively unrelated to the type of integrated detector, our approach is compatible with a range of alternative photodetector device architectures, including bariode devices such as nBn[27] or CBIRD[5] detectors, which could significantly improve noise performance and which would be less susceptible to parasitic contact absorption. The monolithic integration of epitaxial plasmonic materials with infrared optoelectronic elements, proposed and demonstrated in this work, offers a powerful new approach for the design of LWIR photodetectors. For example, with a careful choice of grating coupler, the presented approach could easily be extended to couple into a surface-plasmon-polariton mode and, therefore, an even more significant field enhancement. Strong enhancement of absorption, straightforward control over the spectral position of the absorption peak, and the potential for integration with low-noise detector architectures opens the door to a new class of low noise and high efficiency LWIR detectors for a range of spectroscopic, sensing, and imaging applications.

METHODS

Fabrication. Our detector structures are grown by molecular beam epitaxy in a Varian Gen-II system with effusion sources for gallium, indium, aluminum, silicon, and beryllium and valved cracker sources for arsenic and antimony. All detectors are grown on unintentionally doped (UID, p-type) GaSb substrates. Following a 200 nm GaSb buffer, 144 periods (786 nm) of n^{++} ($\sim 2.7 \times 10^{19}$ cm^{-3}) or n ($\sim 3.4 \times 10^{18}$ cm^{-3}) doped midwave infrared (MWIR) InAs/InAs$_{0.66}$Sb$_{0.34}$ T2SL are grown to form the virtual substrate. The period of the MWIR T2SL is 5.46 nm, with InAs/InAsSb ratio 13.2/4.7 ML. A MWIR T2SL was grown in lieu of a bulk InAsSb alloy as lattice matching the MWIR T2SL to the underlying GaSb and overgrown LWIR T2SL is less demanding than lattice matching to a bulk ternary alloy.[28] The p-i-n InAs/InAs$_{0.39}$Sb$_{0.61}$ LWIR T2SL structures are then grown above the virtual substrate layers. Each sample presented in this work uses the same LWIR T2SL structure, with period 12.5 nm for the $d = 1.42$ μm detector and 12.74 nm for the $d = 1.80$ μm detector, the InAs/InAsSb ratio is 35/6 ML. The detectors designed for $\lambda = 8$ and 10 μm absorption enhancement differ only in the thickness of their intrinsic region. In each of the four detectors, the p-region consists of 9 periods ($\sim$110 nm) of the LWIR T2SL, doped with Be to 1×10^{18} cm^{-3}, and the n-region is 12 periods of LWIR T2SL ($\sim$150 nm), doped with Si to 3×10^{18} cm^{-3}. The i-region is undoped and consists of 93 periods (1.16 μm) of LWIR T2SL for the $d = 1.42$ μm detectors and 120 periods (1.50 μm) of LWIR T2SL for the $d = 1.80$ μm detectors. Following growth, crystal quality is confirmed with X-ray diffraction (XRD) and optical quality is confirmed by PL experiments (both presented in the Supporting Information).

The as-grown wafers are then fabricated into photodetector structures. 700 μm × 500 μm mesas are defined using photolithrography and etched 2 μm using a H_3PO_4, $C_6H_8O_7$, and H_2O_2 mixture. After mesa etching, bottom and top contacts are defined with photolithgrapy and Ti/Pt/Au (34/13/170 nm) contacts are deposited. Metal is lifted off using AZ kwik strip and the sidewalls are left unpassivated.

Detector Characterization. Following growth and fabrication, detectors are mounted to copper blocks with indium paste, wire bonded to Au-coated ceramic stand offs, mounted in a cryostat with ZnSe windows, and cooled to 77 K. Spectral response is performed with a rapid-scan FTIR equipped with a KBr beamsplitter and a mid-IR globar source. The light exiting the FTIR is focused onto the detector using a 2" diameter 90° off-axis parabolic with a 6" focal length. The detector's signal is amplified by a SRS 570 preamplifier. To account for the FTIR optics, the p-i-n detectors' raw spectral response is divided by the spectral response from a spectrally flat pyroelectric detector measured with the FTIR in a step-scan mode, with the light incident upon the detector optically modulated by a chopper wheel at 500 Hz. Responsivity of the detectors is measured with a calibrated blackbody source held at 673 K. A mechanical chopper (1 kHz) modulates the light passing through a 5 mm aperture covering the blackbody source and a lock-in amplifier is used to demodulate the detector signal from the preamplifier. A band-pass filter is used to measure the detector responsivity at $\lambda = 9.46$ μm, and the measured responsivity value is employed to scale the measured and normalized spectral response. To convert from measured responsivity to EQE we used the following expression,

$$\mathrm{EQE}(\lambda) = \frac{R(\lambda)}{\lambda}\frac{hc}{e}$$

where $R(\lambda)$ is the responsivity, h is Planck's constant, c is the speed of light, and e is the electron charge. To calculate the broadband enhancement, F, we evaluate the following expression over the LWIR (103−155 meV),

$$F = \frac{\int^{\mathrm{LWIR}} \mathrm{EQE}_{n^{++}}(E)\mathrm{d}E}{\int^{\mathrm{LWIR}} \mathrm{EQE}_{n}(E)\mathrm{d}E}$$

Modeling and Simulation. Reflectance spectra are simulated using a transfer matrix method (TMM). The absorber layer is treated as having a $\alpha_0\sqrt{E - E_g}$ dependence, where the magnitude of α_0 is determined by fitting the simulated absorption to the measured EQE. For the both detectors α_0 used is 4500 cm^{-1}. The T2SL bandgap $E_g = 96.55$ meV(12.7 μm) is determined by the x-intercept of a linear fit at the full width at half max (fwhm) of the long wavelength side of the measured control detector's PL (provided in Supporting Information). For the highly doped and moderately doped MWIR groundplanes, a simple Drude model is used:

$$\epsilon(\omega) = \epsilon_\infty\left(1 - \frac{\omega_p^2}{\omega^2 + i\gamma\omega}\right)$$

The plasma wavelength and scattering rate used to model each of the virtual substrates' (n^{++} and n) permittivity are fit by measuring reflectance from the bottom of the detector mesas, where the T2SL has been etched off and all that remains is the doped-MWIR T2SL (spectra and fit provided in the Supporting Information). For the n^{++} designer metal, the plasma wavelength and scattering rate are determined to be $\lambda_p = 6.8$ μm and $\gamma = 1 \times 10^{13}$ rads/s, respectively. For the moderately doped control structures the plasma wavelength and scattering rate are determined to be $\lambda_p = 13.1$ μm and $\gamma = 1 \times 10^{13}$ rads/s, respectively. The ϵ_∞ used is 12.06, which is a weighted average of the permittivity for the InAs and InSb in the T2SLs, weighted by the composition for lattice-matched InAsSb at 100 K values.[29] The plasma wavelength for each virtual substrate is determined from the reflection spectra using a peak in the second derivative of the angled reflectance spectra, attributed to the Berreman mode, which spectrally aligns with the plasma wavelength for shallow incidence angles.[30] The scattering rate is then used as a fitting parameter. Simulated absorption is computed by multiplying the relative dissipation in a given layer by the total absorption ($A_{\text{total}} = 1 - R - T$),

$$A_{\text{layer}} = A_{\text{total}}\frac{\int_{z_1}^{z_2}|E(z)|^2\text{Im}(\epsilon(\omega))\text{d}z}{\int_{-\infty}^{\infty}|E(z)|^2\text{Im}(\epsilon(\omega, z))\text{d}z}$$

■ ASSOCIATED CONTENT

Supporting Information

The Supporting Information is available free of charge at https://pubs.acs.org/doi/10.1021/acsphotonics.0c00659.

> Reflection spectra from the plasmonic groundplanes and commensurate differential Berreman mode analysis, PL, and XRD (PDF)

■ AUTHOR INFORMATION

Corresponding Author

Daniel Wasserman − *Department of Electrical and Computer Engineering, The University of Texas at Austin, Austin, Texas 78712, United States;* orcid.org/0000-0003-3234-0803; Email: dw@utexas.edu

Authors

Leland Nordin − *Department of Electrical and Computer Engineering, The University of Texas at Austin, Austin, Texas 78712, United States;* orcid.org/0000-0001-7821-2749

Abhilasha Kamboj − *Department of Electrical and Computer Engineering, The University of Texas at Austin, Austin, Texas 78712, United States;* orcid.org/0000-0003-4186-6284

Priyanka Petluru − *Department of Electrical and Computer Engineering, The University of Texas at Austin, Austin, Texas 78712, United States*

Eric Shaner − *Sandia National Laboratories, Albuquerque, New Mexico 87185, United States*

Complete contact information is available at: https://pubs.acs.org/10.1021/acsphotonics.0c00659

Notes

The authors declare no competing financial interest.

■ ACKNOWLEDGMENTS

L.N., A.K., P.P., and D.W. acknowledge support from Lockheed Martin Co.. Additionally, D.W. and L.N. gratefully acknowledge support from the National Science Foundation (ECCS-1926187). This work was partly done at the Texas Nanofabrication Facility supported by NSF Grant NNCI-1542159. This work was also supported by the Laboratory Directed Research and Development (LDRD) program at Sandia National Laboratories. Sandia National Laboratories is a multimission laboratory managed and operated by National Technology and Engineering Solutions of Sandia, LLC, a wholly owned subsidiary of Honeywell International Inc., for the U.S. Department of Energy's National Nuclear Security Administration under Contract No. DE-NA0003525. This paper describes the objective technical results and analysis. Any subjective views or opinions that might be expressed in this paper do not necessarily represent the views of the U.S. Department of Energy or the United States Government.

■ REFERENCES

(1) Smith, D. L.; Mailhiot, C. Proposal for strained type II superlattice infrared detectors. *J. Appl. Phys.* **1987**, *62*, 2545−2548.

(2) Grein, C. H.; Young, P. M.; Ehrenreich, H. Minority carrier lifetimes in ideal InGaSb/InAs superlattices. *Appl. Phys. Lett.* **1992**, *61*, 2905−2907.

(3) Rhiger, D. R. Performance Comparison of Long-Wavelength Infrared Type II Superlattice Devices with HgCdTe. *J. Electron. Mater.* **2011**, *40*, 1815−1822.

(4) Nguyen, B. M.; Hoffman, D.; Delaunay, P. Y.; Razeghi, M. Dark current suppression in type II InAs/GaSb superlattice long wavelength infrared photodiodes with M-structure barrier. *Appl. Phys. Lett.* **2007**, *91*, 163511.

(5) Ting, D. Z.; Hill, C. J.; Soibel, A.; Keo, S. A.; Mumolo, J. M.; Nguyen, J.; Gunapala, S. D. A high-performance long wavelength superlattice complementary barrier infrared detector. *Appl. Phys. Lett.* **2009**, *95*, 023508.

(6) Gautam, N.; Kim, H. S.; Kutty, M. N.; Plis, E.; Dawson, L. R.; Krishna, S. Performance improvement of longwave infrared photodetector based on type-II InAs/GaSb superlattices using unipolar current blocking layers. *Appl. Phys. Lett.* **2010**, *96*, 231107.

(7) Kim, H. S.; Cellek, O. O.; Lin, Z. Y.; He, Z. Y.; Zhao, X. H.; Liu, S.; Li, H.; Zhang, Y. H. Long-wave infrared nBn photodetectors based on InAs/InAsSb type-II superlattices. *Appl. Phys. Lett.* **2012**, *101*, 161114.

(8) Zuo, D.; Liu, R.; Wasserman, D.; Mabon, J.; He, Z. Y.; Liu, S.; Zhang, Y. H.; Kadlec, E. A.; Olson, B. V.; Shaner, E. A. Direct minority carrier transport characterization of InAs/InAsSb superlattice nBn photodetectors. *Appl. Phys. Lett.* **2015**, *106*, 071107.

(9) Yoon, N.; Reyner, C. J.; Ariyawansa, G.; Duran, J. M.; Scheihing, J. E.; Mabon, J.; Wasserman, D. Modified electron beam induced current technique for in(Ga)As/InAsSb superlattice infrared detectors. *J. Appl. Phys.* **2017**, *122*, 074503.

(10) Nolde, J. A.; Kim, M.; Kim, C. S.; Jackson, E. M.; Ellis, C. T.; Abell, J.; Glembocki, O. J.; Canedy, C. L.; Tischler, J. G.; Vurgaftman, I.; Meyer, J. R.; Aifer, E. H. Resonant quantum efficiency enhancement of midwave infrared nBn photodetectors using one-dimensional plasmonic gratings. *Appl. Phys. Lett.* **2015**, *106*, 261109.

(11) Goldflam, M. D.; Kadlec, E. A.; Olson, B. V.; Klem, J. F.; Hawkins, S. D.; Parameswaran, S.; Coon, W. T.; Keeler, G. A.; Fortune, T. R.; Tauke-Pedretti, A.; Wendt, J. R.; Shaner, E. A.; Davids, P. S.; Kim, J. K.; Peters, D. W. Enhanced infrared detectors using resonant structures combined with thin type-II superlattice absorbers. *Appl. Phys. Lett.* **2016**, *109*, 251103.

(12) Montoya, J. A.; Tian, Z.-B.; Krishna, S.; Padilla, W. J. Ultra-thin infrared metamaterial detector for multicolor imaging applications. *Opt. Express* **2017**, *25*, 23343.

(13) Wang, S.; Yoon, N.; Kamboj, A.; Petluru, P.; Zheng, W.; Wasserman, D. Ultra-thin enhanced-absorption long-wave infrared detectors. *Appl. Phys. Lett.* **2018**, *112*, 091104.

(14) Letka, V.; Bainbridge, A.; Craig, A. P.; Al-Saymari, F.; Marshall, A. R. J. Resonant cavity-enhanced photodetector incorporating a type-II superlattice to extend MWIR sensitivity. *Opt. Express* **2019**, *27*, 23970.

(15) Ünlü, M. S.; Strite, S. Resonant cavity enhanced photonic devices. *J. Appl. Phys.* **1995**, *78*, 607−639.

(16) Ginn, J. C.; Jarecki, R. L.; Shaner, E. A.; Davids, P. S. Infrared plasmons on heavily-doped silicon. *J. Appl. Phys.* **2011**, *110*, 043110.

(17) Law, S.; Adams, D. C.; Taylor, A. M.; Wasserman, D. Mid-infrared designer metals. *Opt. Express* **2012**, *20*, 12155.

(18) Law, S.; Liu, R.; Wasserman, D. Doped semiconductors with band-edge plasma frequencies. *J. Vac. Sci. Technol., B: Nanotechnol. Microelectron.: Mater., Process., Meas., Phenom.* **2014**, *32*, 052601.

(19) Nordin, L.; Li, K.; Briggs, A.; Simmons, E.; Bank, S. R.; Podolskiy, V. A.; Wasserman, D. Enhanced emission from ultra-thin long wavelength infrared superlattices on epitaxial plasmonic materials. *Appl. Phys. Lett.* **2020**, *116*, 021102.

(20) Briggs, A. F.; Nordin, L.; Muhowski, A. J.; Simmons, E.; Dhingra, P.; Lee, M. L.; Podolskiy, V. A.; Wasserman, D.; Bank, S. R. Enhanced Room Temperature Infrared LEDs using Monolithically Integrated Plasmonic Materials. *arXiv preprint arXiv:2005.03163* **2020**, na.

(21) Chandola, A.; Pino, R.; Dutta, P. S. Below bandgap optical absorption in tellurium-doped GaSb. *Semicond. Sci. Technol.* **2005**, *20*, 886.

(22) Rogalski, A.; Martyniuk, P.; Kopytko, M. Type-II superlattice photodetectors versus HgCdTe photodiodes. *Prog. Quantum Electron.* **2019**, *68*, 100228.

(23) Li, Y. B.; Stradling, R. A.; Knight, T.; Birch, J. R.; Thomas, R. H.; Phillips, C. C.; Ferguson, I. T. Infrared reflection and transmission of undoped and Si-doped InAs grown on GaAs by molecular beam epitaxy. *Semicond. Sci. Technol.* **1993**, *8*, 101.

(24) Podolskiy's research group, see http://viktor-podolskiy-research.wiki.uml.edu/RCWA for an implementation of the Rigorous Coupled Wave Analysis.

(25) Kadlec, E. A.; Olson, B. V.; Goldflam, M. D.; Kim, J. K.; Klem, J. F.; Hawkins, S. D.; Coon, W. T.; Cavaliere, M. A.; Tauke-Pedretti, A.; Fortune, T. R.; Harris, C. T.; Shaner, E. A. Effects of electron doping level on minority carrier lifetimes in n-type mid-wave infrared InAs/InAs1-xSbx type-II superlattices. *Appl. Phys. Lett.* **2016**, *109*, 261105.

(26) Vurgaftman, I.; Belenky, G.; Lin, Y.; Donetsky, D.; Shterengas, L.; Kipshidze, G.; Sarney, W. L.; Svensson, S. P. Interband absorption strength in long-wave infrared type-II superlattices with small and large superlattice periods compared to bulk materials. *Appl. Phys. Lett.* **2016**, *108*, 222101.

(27) Maimon, S.; Wicks, G. W. nBn detector, an infrared detector with reduced dark current and higher operating temperature. *Appl. Phys. Lett.* **2006**, *89*, 151109.

(28) Ting, D. Z.; Soibel, A.; Khoshakhlagh, A.; Nguyen, J.; Höglund, L.; Keo, S. A.; Mumolo, J. M.; Gunapala, S. D. Exclusion, extraction, and junction placement effects in the complementary barrier infrared detector. *Appl. Phys. Lett.* **2013**, *102*, 1−5.

(29) Gillen, G. D.; DiRocco, C.; Powers, P.; Guha, S. Temperature-dependent refractive index measurements of wafer-shaped InAs and InSb. *Appl. Opt.* **2008**, *47*, 164−168.

(30) Nordin, L.; Dominguez, O.; Roberts, C. M.; Streyer, W.; Feng, K.; Fang, Z.; Podolskiy, V. A.; Hoffman, A. J.; Wasserman, D. Mid-infrared epsilon-near-zero modes in ultra-thin phononic films. *Appl. Phys. Lett.* **2017**, *111*, 091105.